










Cite this: *RSC Adv.*, 2025, 15, 21479

# Design of a Zn-based porphyrin MOF biosensor for fluorometric detection of HER2 as a breast cancer biomarker†

May R. Ibrahim, <sup>a</sup> Shaikha Alneyadi, <sup>a</sup> Khai-Nghi Truong, <sup>b</sup>  
Hesham El- Maghraby, <sup>a</sup> Mohamed Abdellah, <sup>a</sup> Ahmed M. El-Zohry, <sup>c</sup>  
Stefan Wuttke <sup>ad</sup> and Yaser Greish <sup>\*ae</sup>

Human epidermal growth factor receptor 2 (HER2) is a critical biomarker for early detection and diagnosis of breast cancer. In this study, we report the synthesis and characterization of a novel zinc-based metal–organic framework (Zn-MOF) biosensor designed for sensitive and selective fluorometric detection of HER2. The Zn-MOF was synthesized *via* a solvothermal method using a suitable organic ligand to promote fluorescence properties. The synthesized Zn-MOF was characterized using various techniques, including X-ray diffraction (XRD), scanning electron microscopy (SEM), Fourier-transform infrared (FTIR) spectroscopy, and fluorescence spectroscopy, confirming its structure, morphology, and photoluminescent properties. The Zn-MOF exhibited high binding affinity towards HER2, which resulted in a measurable fluorescence quenching directly correlated with HER2 concentration. This Zn-MOF-based biosensor demonstrated excellent sensitivity, with a detection limit of 1.38 pM and good specificity, showing minimal interference from other proteins commonly found in human serum. These results indicate the potential of Zn-MOFs as effective platforms for the development of biosensors for cancer biomarker detection, paving the way for their application in early cancer diagnostics and personalized medicine.

Received 18th March 2025  
Accepted 3rd June 2025

DOI: 10.1039/d5ra01942g

rsc.li/rsc-advances

## Introduction

Cancer is commonly recognized as a leading cause of death globally. It is characterized by irregular and unrestrained multiplication of cells due to the accumulation of genetic and epigenetic abnormalities.<sup>1</sup> Breast cancer ranks as the second most prevalent form of cancer, impacting roughly 200 000 women each year in the United States alone. Early detection of cancer is crucial for monitoring treatment progress and cancer development, thereby improving treatment efficacy and preventing recurrence in patients. Recently, the examination of cancer protein biomarkers has demonstrated promise in the monitoring and diagnosis of various cancer types. One specific

biomarker, overexpressed in 20–30% of human breast cancers, is human epidermal growth factor receptor 2 (HER2, also known as neu or ErbB2). The HER2 structure is schematically depicted in Scheme 1a, as obtained from the protein bank database (PDB). Monitoring of HER2 is crucial due to its association with highly aggressive forms of breast cancer and the elevated risk of recurrence in patients, often correlated with these tumors.<sup>2</sup> The extracellular domain (ECD) of HER2 is released into the blood, its level increases during metastasis, and 15% of primary breast cancer patients have elevated levels of serum HER2 ECD.<sup>3</sup>

Currently, many methods have been reported for the detection of breast cancer biomarkers. These include surface plasmon resonance (SPR), chemiluminescence (CL), surface-enhanced Raman scattering (SERS), opto-fluidic ring resonator and electrochemical methods, in addition to the conventional enzyme-linked immunosorbent assay (ELISA) method.<sup>4</sup> Despite their accuracy in detection, many established assays are deemed complex, time-intensive, and expensive. Recently, biosensors have been introduced as a promising, selective, and economical alternative to conventional methods for detecting cancer biomarkers. Biosensors are analytical devices that combine a biological component (recognition part) with a transducer (mainly a nanostructure material) to generate signals that can be detected to monitor specific biological

<sup>a</sup>Department of Chemistry, UAE University, Al Ain, 15551, United Arab Emirates.  
E-mail: y.alfiti@uaeu.ac.ae

<sup>b</sup>Rigaku Europe SE, Hugenottenallee 167, 63263 Neu-Isenburg, Germany

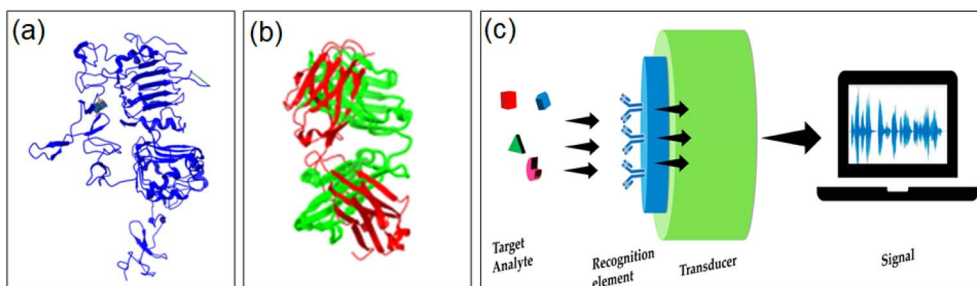
<sup>c</sup>Ultrafast Laser Spectroscopy Lab, Center for Integrative Petroleum Research, King Fahd University of Petroleum and Minerals, Dhahran 31261, Saudi Arabia

<sup>d</sup>Academic Centre for Materials and Nanotechnology, AGH University of Krakow, Krakow, 30-059, Poland

<sup>e</sup>Zayed Centre for Health Sciences, United Arab Emirates University, Al-Ain, 15551, United Arab Emirates

† Electronic supplementary information (ESI) available. CCDC 2333780. For ESI and crystallographic data in CIF or other electronic format see DOI: <https://doi.org/10.1039/d5ra01942g>





Scheme 1 HER2 protein structure (a), trastuzumab (b), and biosensor parts (c).

substances. Scheme 1c illustrates the structure of a typical biosensor. There are several types of biosensors, categorized based on their detection principles as optical, electrochemical, piezoelectric, *etc.*<sup>5</sup>

Several nanostructures have been employed to synthesize the transducer part of a typical HER2 biosensor. Among these nanostructures, metal–organic frameworks (MOFs) have been considered for the design of biosensors. MOFs are porous structured materials characterized by their crystalline nature and high surface area, consisting of metal-based nodes (which can be ions or clusters) connected to organic linkers through coordination bonds. These materials exhibit distinctive physical and chemical characteristics.<sup>6</sup> Several studies have been reported, primarily focusing on the applications of bulk MOF crystals and 3D MOF materials in the fabrication of biosensors. Nevertheless, it is only in recent times that there has been a notable increase in research concerning the use of 2D MOFs for various applications. 2D MOFs exhibit numerous intriguing characteristics that make them well-suited for use in sensing applications. The presence of exposed metal sites on the 2D MOF's surface enhances the rate of surface reactions. These exposed metal sites with their exceptional quenching properties render them suitable for electrochemical, optical and fluorometric immunosensors, thereby increasing the biosensor sensitivity.<sup>6,7</sup>

Several studies have been reported, primarily focusing on the use of bulk MOF crystals and 2D, 3D MOF materials in biosensor fabrication; recent studies have demonstrated their successful application as fluorescent sensors for detecting metal ions, antibiotics, and biomolecules with high sensitivity and rapid response times.<sup>8–12</sup> Fluorescence biosensing has been presented as an accurate and simple technique. Fluorometric biosensors utilize the fluorescence properties of specific molecules to detect and quantify specific biological substances or processes.<sup>13</sup> Many fluorescent compounds have been considered for the design of biosensors. MOF-based fluorescence sensors are more chemically tunable as compared to other fluorescent nanomaterials.<sup>14–22</sup> The unique tunable chemical functionality of MOFs is a highly recognized property that is expected to facilitate an efficient and specific host–guest recognition. Moreover, the presence of  $\pi$  and  $n$  electrons along the organic linker of the MOF structure contributes to the formation of excellent and variable fluorescence signals.<sup>23–25</sup> In addition, the intrinsic chemical functionality of MOFs makes

them tuneable for decoration with other nanomaterials, facilitating the detection of molecules with higher efficiency.<sup>26–30</sup>

Porphyrins, which are a group of organic compounds known for their ring-like structure and ability to complex with metal ions, represent an important class of fluorescent compounds. Porphyrins are commonly found in natural molecules, such as hemoglobin and chlorophyll, and they exhibit unique optical properties, including fluorescence, when excited by light. Porphyrin fluorescent MOFs, therefore, refer to a type of porous MOFs that incorporates porphyrin molecules as linkers, which exhibit optical and fluorescence properties in a MOF structure.<sup>31</sup>

By synergistically harnessing the distinctive attributes of 2D MOFs and the remarkable optical characteristics inherent to porphyrin molecules, a highly proficient fluorescence biosensor can be fabricated. Practically, numerous studies in the literature have documented the successful utilization of 2D porphyrin-based MOFs in the construction of biosensors for detecting different analytes.<sup>32–34</sup>

For the biorecognition part of the HER2 biosensor, Herceptin, known by its generic name trastuzumab, has been used to detect elevated HER2 expression.<sup>35–37</sup> The structure of trastuzumab is shown in Scheme 1b, as derived from the PDB. Trastuzumab is a monoclonal human antibody created through the recombinant DNA (rDNA) technology. It is designed to precisely target the ECD of the HER2 protein, with the aim of interfering with or stopping its growth.

Herewith, we present our research on the application of a Zn-based 2D porphyrin MOF as a fluorometric biosensor for the ultrasensitive and highly selective detection of HER2 antigen with high efficiency. To achieve this, we utilized TCPP (5,10,15,20-tetra (4-carboxyphenyl) porphyrin), a member of the porphyrin family (Fig. S1†), to synthesize fluorescing 2D Zn-TCPP MOF, while trastuzumab was used as the recognition element. In our extensive evaluation encompassing fluorescence detection and selectivity tests, Zn-TCPP MOF demonstrated its remarkable ability in achieving ultrasensitive and quantitative detection of HER2, while effectively excluding interferences from other compounds commonly present in plasma and body fluids from the targeted antigen. Moreover, while the existing novel MOF-based technique surpasses the commercially available ELISA kits for HER2 determination, our developed Zn-TCPP MOF-based detection assay has demonstrated a significantly improved performance with an



impressively low detection limit of just 1 picogram per milliliter ( $1 \text{ pg mL}^{-1}$ ).

## Materials and methods

### Materials

Zinc nitrate hexahydrate ( $\text{Zn}(\text{NO}_3)_2 \cdot 6\text{H}_2\text{O}$ , 99%), terephthalaldehydic acid, pyrrole, ascorbic acid, glutathione, dopamine, glutamic acid, bovine serum albumin (BSA), ethyl(dimethylaminopropyl)carbodiimide (EDC), *N*-hydroxysuccinimide (NHS), and cysteine were purchased from Sigma Aldrich. HER2 (CD340) was purchased from Sino Biologicals, and anti-HER2-Tra-hIgG1(Trastuzumab) was provided by InvivoGen. All chemical reagents used in the experiments were analytically pure. Ultrapure water from the Milli-Q purified system was used for all preparations.

### Synthesis of the 5,10,15,20-tetrakis-(4-carboxyphenyl)-21,23H-porphyrin (TCPP) linker

A microwave method was used for the synthesis of the TCPP linker, following the work of Sadeghi *et al.*<sup>38</sup> and Wang *et al.*<sup>39</sup> with slight modifications. An equimolar portion of pyrrole (0.2 mL, 0.193 g, 2.88 mmol) and terephthalaldehydic acid (0.3380 g, 2.25 mmol) were mixed with an excess of propionic acid (100 mL, 99.3 g, 1.34 mol). The solution was stirred at 90 °C for 90 min under 100 W in an argon atmosphere in a microwave oven. A deep purple suspension was obtained. After the reaction was completed, the solution was left to cool down. The solution was then filtered and rinsed with methanol. After being allowed to dry in air, the precipitate was collected as a dark purple powder in a 40.0 mg yield.

### Synthesis of 2D Zn-TCPP MOF

The synthesis method of Zn-TCPP MOF has been previously reported.<sup>35</sup> We have adopted this method with minor modifications. Typically, 2.0 mg TCPP was first dissolved in dimethylformamide (DMF) (10 mL) (0.00254 millimoles), followed by ultrasonic treatment for 1 min. 8.0 mg of  $\text{Zn}(\text{NO}_3)_2 \cdot 6\text{H}_2\text{O}$  was added to 5 mL of ethanol (0.0203 millimoles). Both solutions were mixed together and ultrasonicated for 2 min to ensure complete solubility of the solid content. Then, the mixture was kept under heating and stirring at 120 °C for 2 hours. The mixture was then slowly cooled to room temperature, where a glittery like purple/red precipitate was formed. The precipitate was separated by centrifuging at 6000 rpm for 10 minutes. Finally, the obtained product (0.4 mg yield) was washed three times with ethanol and dried at 60 °C under vacuum for 24 h.

### Characterization of the Zn-TCPP MOF nanostructure

The detailed crystal structure of the as-prepared Zn-TCPP MOF structure was investigated using continuous rotation three-dimensional electron diffraction (3D ED). Microcrystalline powder of Zn-TCPP was spread on a standard lacey-carbon-coated copper TEM grid (Fig. S2†). Red plate-like crystallites with a thickness of a few 100 nm were selected for the 3D-ED/microED measurements. Cryo-transfer, *i.e.*, freezing of

samples prior to introduction to vacuum, at 100 K using a Gatan ELSA (Model 698) specimen holder, was applied here. As electron diffraction requires samples to be studied under high vacuum, the cryo-transfer technique is essential for many sensitive compounds, such as solvent-containing MOFs or proteins. In addition to stabilization *in vacuo*, other benefits include improving the resolution, reducing disorder, reducing beam damage, and prolonging the general lifetime of the sample, respectively.

Electron diffraction measurements for Zn-TCPP were conducted using the Rigaku XtaLAB Synergy-ED, equipped with a Rigaku HyPix-ED detector optimized for operation in the continuous rotation 3D-ED experimental setup.<sup>17,18</sup> Data acquisition was performed at 100 K under high vacuum with an electron wavelength of 0.0251 Å (200 kV). The diffraction data were processed in the program CrysAlis<sup>Pro</sup>.<sup>40</sup> A multi-scan absorption correction was performed using spherical harmonics implemented in the SCALE3 ABSPACK scaling algorithm in CrysAlis<sup>Pro</sup>. The structure was solved using ShelXT,<sup>41</sup> and subsequently refined with kinematical approximation using ShelXL<sup>42</sup> in the crystallographic program suite Olex2.<sup>43,44</sup> By merging the data of two individual grains/datasets of Zn-TCPP, a completeness of 99.0% up to a resolution of 0.80 Å was achieved. A solvent mask was calculated, and 66 electrons were found in a volume of 463 Å<sup>3</sup> in two voids per unit cell. This corresponds to one highly disordered co-crystallized DMF as well as one EtOH molecule per unit cell. Non-hydrogen atoms were assigned anisotropic displacement parameters. The hydrogen atoms bonded to oxygen atoms were located from Fourier difference maps. Other hydrogen atoms were placed in idealized positions and included as riding. Isotropic displacement parameters for all H atoms were constrained to multiples of the equivalent displacement parameters of their parent atoms with  $U_{\text{iso}}(\text{H}) = 1.2 U_{\text{eq}}(\text{parent atom})$ . Enhanced rigid bond restraints<sup>45,46</sup> with standard uncertainties of 0.001 Å<sup>2</sup>, as well as distance restraints (DFIX), were applied. The experimental and refinement details are given below. CCDC 2333780 contains the supplementary crystallographic data for this study. These data can be obtained free of charge via [https://www.ccdc.cam.ac.uk/data\\_request/cif](https://www.ccdc.cam.ac.uk/data_request/cif), or by emailing [data\\_request@ccdc.cam.ac.uk](mailto:data_request@ccdc.cam.ac.uk), or by contacting The Cambridge Crystallographic Data Centre, 12 Union Road, Cambridge CB2 1EZ, UK; fax: +44 1223 336033.

The prepared Zn-TCPP MOF nanostructure was also characterized for its structure using a Rigaku MiniFlex XRD, thermogravimetric analysis (TGA), and a Nexus FTIR technique. The morphology of the Zn-TCPP MOF was evaluated using a field emission SEM, FEI Inspect F50, USA), equipped with an energy dispersive spectroscopy (EDS) unit for the elemental analysis of the Zn-TCPP MOF powder. The BET (Brunauer–Emmett–Teller) analysis was performed using a micrometrics instrument. The adsorption–desorption experiment was measured at a relative pressure ( $P/P_0$ ) between 0.05 and 0.30.

The fluorescence and absorbance properties of Zn-TCPP MOF were measured using a Horiba UV-vis spectrometer. In brief, 1 mg of the Zn-TCPP MOF sample was added to 20 mL of ultrapure water and mixed evenly to form a stable solution.



Then, 3 mL of the above solution was measured at a wavelength range of 200–800 nm. The time scanning mode and slit of the instrument were adopted to collect the fluorescence values for Zn-TCPP MOF with different solvents (including acetone, ethanol, water, and ethylene glycol) in a fixed concentration of 0.5 mg mL<sup>-1</sup> at 424 nm (the slit of excitation and emission is 5 nm, and the voltage is 600 V) to select the optimum concentration of Zn-TCPP MOF to be used for detection.

### Bioconjugation of Zn-TCPP MOFs with trastuzumab

In brief, 10 mg of the synthesized Zn-TCPP was dispersed in 15 mL of deionized water and activated by the addition of 10 µL of 100 mM EDC and 20 µL of 100 mM NHS under stirring for 15 min. Subsequently, 100 µL of 500 µg mL<sup>-1</sup> trastuzumab was added to the solution with stirring for 2 hours at room temperature. To ensure the complete immobilization of the protein, the reaction solution was kept under stirring at room temperature overnight. Excess NHS-active sites of the Zn-TCPP MOF were then blocked with 1% BSA solution for 2 h. After centrifugation and washing to remove unbound biomolecules, the Zn-TCPP@Trastuzumab (biosensor) assembly was finally resuspended in 2 mL of deionized water and stored at 4 °C for further use.

### Characterization of the Zn-TCPP@Trastuzumab biosensor

The prepared biosensor was further characterized using various techniques to confirm the structure and morphology of the Zn-TCPP@Trastuzumab structure owing to trastuzumab coupling. These included XRD, FTIR, TGA, EDS, fluorescence, absorbance, and emission excitation map (EEM) for the Zn-TCPP MOF before and after functionalization with trastuzumab, *i.e.*, Zn-TCPP@Trastuzumab (biosensor).

### Time-correlated single photon counting (TCSPC) experiment for pure Zn-TCPP and biosensor.

The fluorescence lifetime measurements were performed using a PicoQuant MicroTime 200 time-resolved confocal microscope system. A pulsed diode laser (LDH-D-C-405, PicoQuant) emitting at 415 nm with a pulse duration of 70 ps and a repetition rate of 40 MHz was used for the excitation. Emitted photons were detected using a single-photon avalanche diode (SPAD, PDM Series, Micro Photon Devices), and the timing was recorded using a PicoHarp 300 time-correlated single photon counting module. Solutions of both the pure Zn-TCPP MOF and Zn-TCPP loaded with the antibody, *i.e.*, Zn-TCPP@Trastuzumab, were prepared in ethanol (HPLC grade, Merck) at a concentration of 1 mM and further diluted to 1 µM in phosphate-buffered saline (PBS, pH 7.4). All other reagents were of analytical grade and used as received. The photon counts were accumulated until a peak count of 10 000 was achieved, ensuring a sufficient signal-to-noise ratio. The fluorescence decay curves were analyzed using the SymPhoTime 64 software (PicoQuant). The decay data were fitted to a single-exponential model using a least-squares fitting algorithm. The quality of the fit was assessed using the chi-square ( $\chi^2$ ) test and the residuals analysis.

### Procedure of the immunoassay (detection of HER2), calibration curve construction and limit of detection (LOD) calculations

The immunoassay of HER2 detection was established in 12 concentrations (1, 10, 50, 100, 150, 200, 250, 300, 350, 400, 450, 500 picogram per mL (pg mL<sup>-1</sup>)). Typically, serial dilutions of the antigen were prepared in a PBS solution, then the biosensor (Zn-TCPP-trastuzumab conjugate) was introduced in a fixed concentration for each sample. After incubation, the fluorescence signals were recorded for each concentration at an excitation wavelength of 424 nm, voltage of 600 V and slit width of 5 nm.

### Selectivity of the proposed Zn-TCPP@Trastuzumab sensor

Six common substances in the blood (glutamic acid, glucose, albumin, arginine, dopamine, cysteine, and ascorbic acid) were selected to confirm the specific binding of the biosensor to HER2. A single concentration of the antigen was chosen (100 Pg mL<sup>-1</sup>) and was mixed with each metabolite in a separate tube. Afterwards, the fluorescence signals of the different samples were compared and analyzed. These experiments were carried out at room temperature.

### Molecular docking between trastuzumab and the secondary building unit (SBU) of the Zn-TCPP MOF nanostructure

The crystal structure information for the SBU of the Zn-TCPP MOF was obtained from the 3D ED data collected using a Rigaku diffractometer. Mercury software was used to convert the CIF file to the PDB format. The PDB was used to obtain the structure of trastuzumab (ID-6MH2), which is known to consist of two chains (A and B). The ChimeraX visualization software was used to view the three-dimensional structures of the protein chain and the MOF SBU.

The CB-DOCK molecular docking server, which is based on the principles of shape complementarity, was used to dock trastuzumab as a receptor and Zn-TCPP as a ligand. The docked complex with the lowest energy was then visualized and analyzed for possible binding sites using ChimeraX.

## Results and discussion

### Characterization of Zn-TCPP MOF and Zn-TCPP@Trastuzumab nanostructures

After slow evaporation of the DMF/EtOH solution of Zn-TCPP, a red microcrystalline solid was obtained. The solid-state structure of these crystals was elucidated using continuous rotation 3D electron diffraction (3D ED; see Fig. 1a and b).<sup>37,38</sup> Zn-TCPP crystallizes in the monoclinic space group *P2<sub>1</sub>/m* with the composition [ $\{Zn-TCPP\}Zn_2(H_2O)_2$ ] and a unit cell volume of 1332(54) Å<sup>3</sup>. In 2018, an isostructural and isomorphous MOF compound was reported by Urtizberea *et al.*,<sup>47</sup> namely a 2D mixed-metal coordination compound with a composition of [ $\{CuTCPP\}Zn_2(H_2O)_2$ ], as determined by SCXRD. More recently, an isostructural monometallic Zn(II) metal-organic framework (Zn-TCPP) was reported by Zhu and co-workers.<sup>48</sup> Zn-TCPP forms a 2D layered structure, as depicted in Fig. 1c. The





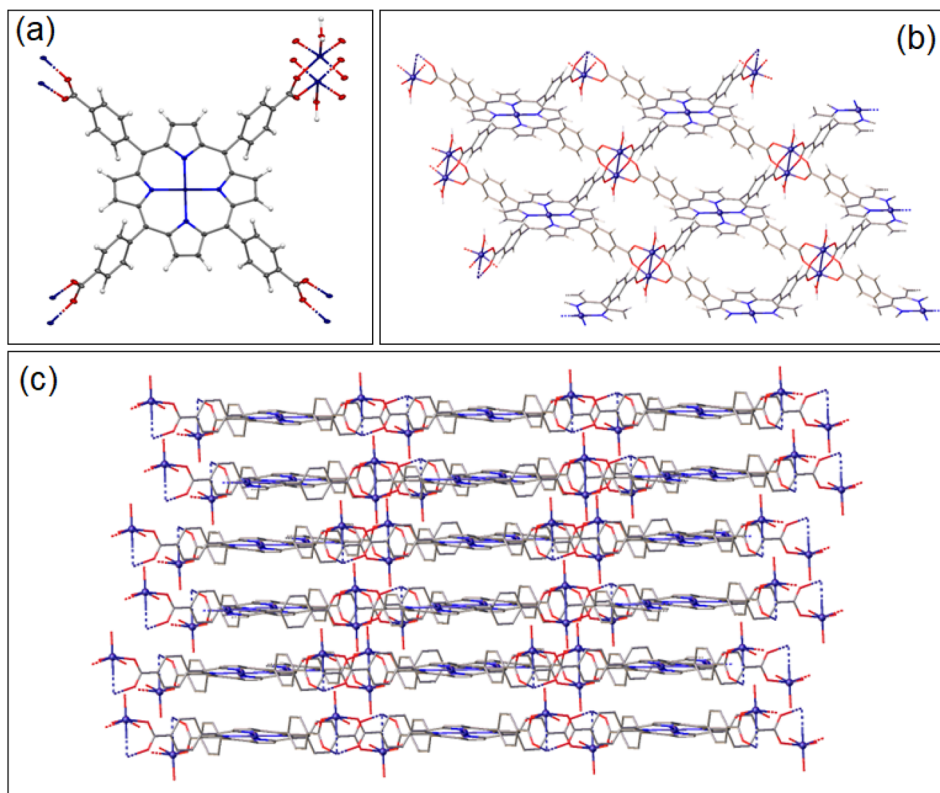


Fig. 1 (a) 3D ED structure of the asymmetric unit of ZnTCPP. Displacement ellipsoids are drawn at a 50% probability level; (b) one layer of the extended 2D structure; and (c) crystal packing of the 3D hydrogen-bonded coordination polymer ZnTCPP viewed along the [010] direction. Co-crystallized solvent molecules (EtOH, DMF) and hydrogen atoms have been omitted in the latter two figures for clarity.

structure is stabilized by intermolecular TCPP-water interactions, *i.e.*, O–H...O hydrogen bonds, forming an extended 3D hydrogen-bonded network (see Fig. S3 and S4†).

Fig. 2a shows the XRD pattern of the as-prepared Zn-TCPP MOF, as compared with the simulated pattern of the Zn-TCPP single crystal. The 2D Zn-TCPP MOF exhibited four typical peaks in the XRD spectrum, which are in accordance with the monoclinic structure of Zn-TCPP MOF. Compared with the simulated XRD pattern of a Zn-TCPP single crystal, an additional peak representing the (200) diffraction was observed at a  $2\theta$  value of  $10.6^\circ$ . This is attributed to the preferential orientation of the Zn-TCPP 2D crystallites in the sample powder, as was previously mentioned by Zhou *et al.*<sup>49</sup> Hence, the XRD pattern of the as-prepared Zn-TCPP indicates its purity and confirms its 2D morphology, consistent with the SEM micrograph of the material.

The FT-IR spectra of the as-prepared Zn-TCPP and pure TCPP linker are shown in Fig. 2b. For the TCPP linker, a broad band at  $3396\text{ cm}^{-1}$  was credited to stretching of O–H/N–H groups of the linker. The stretching vibrations at  $3396$  and  $1703\text{ cm}^{-1}$  were due to the O–H and C=O groups of the carboxylic acid group, and the bands at  $1402\text{ cm}^{-1}$  were the typical absorption of C=C of the benzene ring. The FT-IR spectrum of the Zn-TCPP MOF showed a band at  $1604\text{ cm}^{-1}$ , which is shifted as compared with that of the TCPP ligand at  $1703\text{ cm}^{-1}$ , which could be attributed to the formation of a coordinated bond between the metal

cations and the  $\text{COO}^-$  group of the TCPP ligands.<sup>50</sup> In addition, the broad band at  $3396\text{ cm}^{-1}$  of the TCPP linker was shown as a narrow band in the FT-IR spectrum of Zn-TCPP MOF and is attributed to the transformation of the –COOH groups into the  $\text{Zn}(\text{COO})_2$  coordinated structure.

Fig. 2c and S5† show the TGA and DTG thermograms, respectively, of the Zn-TCPP MOF nanostructure as compared with those of the pure TCPP linker. Three thermal events were observed in the TGA and DTG thermograms of the TCPP linker at  $50^\circ\text{C}$ ,  $82^\circ\text{C}$ , and  $367^\circ\text{C}$ . These events correspond to the removal of weakly adsorbed water and solvent (ethanol and DMF) molecules at  $50^\circ\text{C}$  and  $82^\circ\text{C}$ , respectively, and the degradation and decomposition of the TCPP structure at  $367^\circ\text{C}$ . In contrast, the TGA and DTG thermograms of the Zn-TCPP MOF structure showed 5 thermal events with peaks at  $41^\circ\text{C}$ ,  $97^\circ\text{C}$ ,  $191^\circ\text{C}$ ,  $448^\circ\text{C}$  and  $481^\circ\text{C}$ . These correspond to the removal of weakly adsorbed water and solvent molecules below  $100^\circ\text{C}$ , removal of the entrapped solvent molecules at  $191^\circ\text{C}$ , and degradation of the MOF structure at  $448$  and  $481^\circ\text{C}$ , respectively. These findings confirm the Zn-TCPP MOF structure formed through the binding of  $\text{Zn}^{2+}$  ions to the high electron density –N and –NH groups of the TCPP linker molecules.

The ultraviolet-visible (UV-vis) spectrum of Zn-TCPP, as compared to that of the pure TCPP linker, is shown in Fig. 2d. The UV-vis spectrum of the TCPP linker shows the standard Soret band and four Q bands. The Soret band at  $416\text{ nm}$  is the

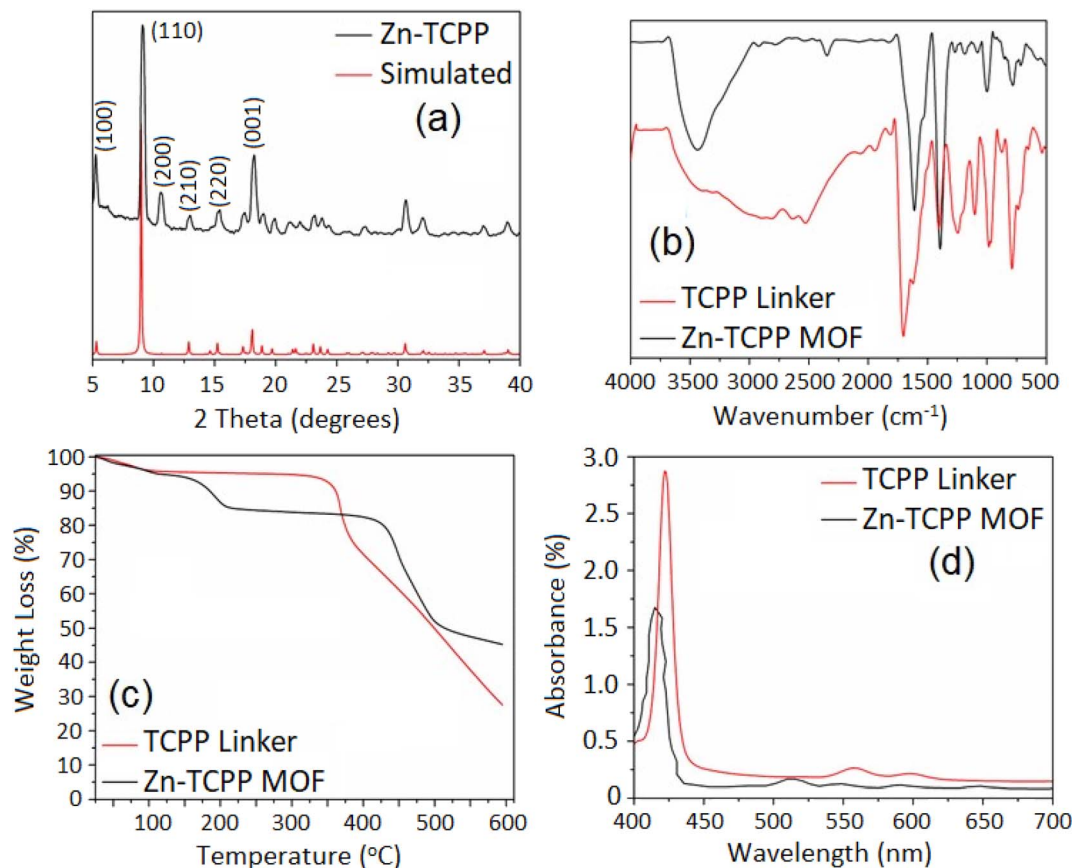


Fig. 2 XRD pattern (a), FTIR spectrum (b), TGA-DTG thermograms (c), and UV-vis spectra (d) of the as-prepared Zn-TCPP MOF structure.

characteristic peak of the porphyrin ring in the free TCPP ligand, whereas it shows a slight red shift (424 nm) in the case of the Zn-TCPP MOF nanosheet. The free TCPP ligand exhibits four Q bands at 512, 546, 590 and 645 nm, while the Zn-TCPP nanosheet displays two predominant Q bands at 558 and 596 nm, respectively, which show the effective metalation of the porphyrin rings by  $\text{Zn}^{2+}$  cations.

The Zn-TCPP MOF structure exhibited a type V Langmuir isotherm, as shown in Fig. S6,<sup>†</sup> which is an indication of its 2D nature and the possibility of multilayer adsorption of  $\text{N}_2$  gas

onto its surfaces. This type of isotherm is characteristic of materials with pores that are not easily accessible and may involve capillary condensation in mesopores. The adsorption at higher pressures suggests the filling of larger pores or capillaries. Despite the 2D nature of the Zn-TCPP MOF structure, it exhibited a BET surface area of  $870 \text{ m}^2 \text{ g}^{-1}$ . Fig. S7<sup>†</sup> also shows the pore size distribution of Zn-TCPP 2D MOF. The pore size distribution data specify that Zn-TCPP has a micropore size distribution of 1.35 nm, which is close to the value of 1.6 nm based on crystallographic data.<sup>48</sup> In addition, the 2D MOF BET

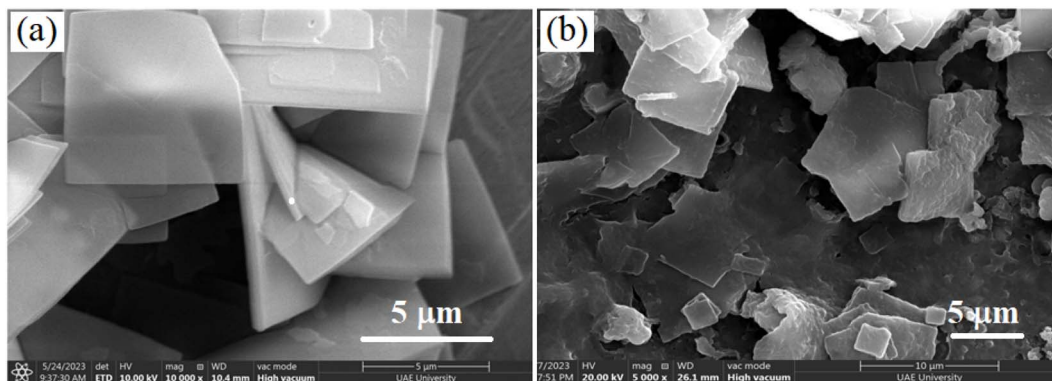


Fig. 3 SEM micrographs of (a) Zn-TCPP and (b) Zn-TCPP@Trastuzumab nanosheets.



hysteresis shows a lowering in the volume of nitrogen at high pressure values, which could be attributed to the nature of the 2D structures that form slit-like pores during the aggregation of Zn-TCPP nanosheets in vacuum drying. Also, this may be attributed to the bottle-shaped pores, which are also one of the characteristics of a type V isotherm.

The morphology of the as-prepared Zn-TCPP was evaluated using the SEM-EDX technique. Results are shown in Fig. 3a, S8a and S9a†. The SEM micrographs of the as-prepared Zn-TCPP MOF structures reflect their 2D morphology with sizes ranging from hundreds of nanometers to several micrometers. Moreover, Fig. 3a shows the flexibility of the Zn-TCPP sheet structure, where the arrangement of sheets with respect to each other resulted in a pronounced bending of the Zn-TCPP sheets. The elemental analysis of the as-prepared Zn-TCPP is shown in Fig. S9a† and indicates the presence of C, N, O and Zn with approximate atomic concentrations of 55.05%, 14.62%, 23.73% and 4.62%, respectively.

Fig. 3b, S8b and S9b† show the SEM micrographs and EDX pattern of the optimally prepared Zn-TCPP@Trastuzumab nanosheets. The morphology of the Zn-TCPP 2D flakes was slightly maintained upon the immobilization of Trastuzumab molecules, where signs of surface deformity were observed, as shown in Fig. 3b. A homogeneous distribution of Zn-TCPP@Trastuzumab flakes is shown in Fig. S8b.† The elemental analysis of the Zn-TCPP@Trastuzumab structure shown in Fig. S9b† confirmed the presence of C, O, S, and Zn elements with atomic percentages of 46.3%, 20.16%, 2.04% and 4.1%, respectively. The presence of the S peak in the EDS spectrum of the Zn-TCPP@Trastuzumab structure is further evidence of the immobilization of trastuzumab into/onto the Zn-TCPP MOF structure.

The immobilization of trastuzumab was further confirmed *via* the broadening of the bands at  $3400\text{--}3250\text{ cm}^{-1}$  and  $1600\text{--}1700\text{ cm}^{-1}$ , which are related to the presence of O–H/N–H and the amide (C–N) groups, respectively. In addition, a band at  $1203\text{ cm}^{-1}$  in the Zn-TCPP@Trastuzumab FTIR spectrum (Fig. 4a) is attributed to the C–N bond that can be found between Zn-MOFs and the antibody, as well as the C–N bonds in the protein molecules.<sup>6</sup> Fig. 4b and S10† show the TGA and DTG thermograms, respectively, of the Zn-TCPP@Trastuzumab as compared with the as-prepared Zn-TCPP MOF structures. The former showed the presence of thermal events with peaks at  $51^\circ\text{C}$  and three events at 221, 307 and  $327^\circ\text{C}$ . These are related to

the removal of weakly adsorbed water molecules at  $51^\circ\text{C}$  and the subsequent removal and decomposition of the Trastuzumab drug. Two major thermal events were observed at 436 and  $488^\circ\text{C}$ , which correspond to the decomposition of the remaining Zn-TCPP MOF structure and the degradation of the TCPP porphyrin structure. Compared with an overall weight loss of 55% for the decomposition of the as-prepared Zn-TCPP MOF structure, the Zn-TCPP@Trastuzumab structure showed an overall weight loss of 87%, confirming the successful loading of the drug into/onto the Zn-TCPP MOF structure.

The photoactivity of Zn-TCPP and Zn-TCPP@Trastuzumab structures were evaluated using fluorescence measurements. During these measurements, various common organic solvents, such as methanol, ethanol, ethylene glycol, and water, were used to disperse the Zn-TCPP MOF. After optimizing the experiment, water was chosen to conduct the biosensing assay to ensure the safety and biocompatibility with body fluids. Results are shown in Fig. 4c. Zn-TCPP MOF presented an emission band in the range of  $500\text{--}800\text{ nm}$  when excited by light ( $424\text{ nm}$ ), with the strongest peak observed at  $660\text{ nm}$ . The fluorescence behavior of the Zn-TCPP MOF could be attributed to the ligand-to-metal charge transfer (LMCT).<sup>48</sup> Meanwhile, the steady-state fluorescence spectrum of the Zn-TCPP@Trastuzumab structure was red-shifted in comparison with the Zn-TCPP MOF structure (Fig. 4c). This is because the electronic conjugation between the MOF's ligands and the amino acids of the protein can change. This can lower the energy gap between the ground state and the excited state of the fluorescent ligands, resulting in a red shift (emission at longer wavelengths). Fluorescence of the Zn-TCPP@Trastuzumab biosensor retained its prevalent PL characteristics of pure MOF with the emission peaks at  $610$  and  $660\text{ nm}$ . However, after its bioconjugation with trastuzumab, the PL intensity showed a slight decrease in intensity due to quenching. This quenching may be justified by the peripheral  $\text{--COOH}$  groups forming the bioconjugation bonds with the added protein. Besides, a blue shift occurred after the conjugation, which could be attributed to the energy transfer processes between the non-fluorescent molecules and the fluorophores, which can lead to a redistribution of energy levels. If energy transfer occurs preferentially to higher-energy states of the fluorophores, it can result in a blue shift in the emission spectrum.<sup>51</sup>

Generally, MOFs built with organic photoactive ligands could reduce the aggregation-caused quenching (ACQ) effect

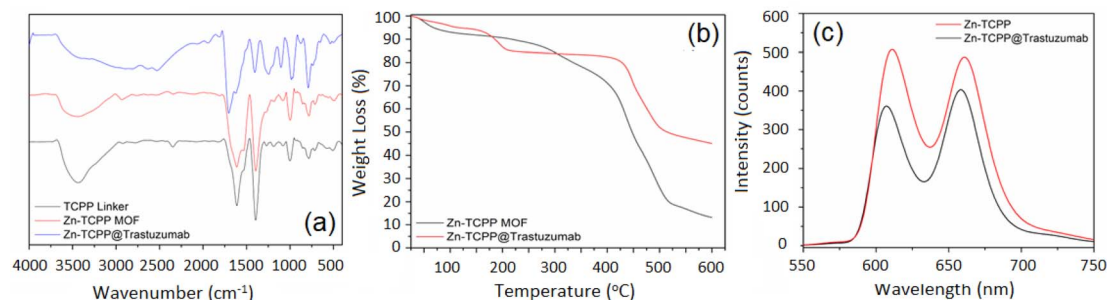


Fig. 4 FTIR spectra (a), TGA thermograms (b), and photoluminescence (PL) spectra (c) of Zn-TCPP and TCPP@Trastuzumab nanosheets.



faced by most organic photoactive ligands alone, as the porous framework arranges these photoactive ligands in an intra-molecular framework structure. MOFs constructed with organic photoactive ligands, such as TCPP, effectively address the ACQ effect, which is a common issue where the fluorescence of organic molecules diminishes when they aggregate. This quenching occurs because, in close proximity, these molecules can undergo non-radiative energy transfer or form non-emissive aggregates, reducing their luminescence. In MOFs, the photoactive ligands are integrated into a crystalline, porous framework. This framework provides a structured environment that spatially separates the ligands at a molecular level, preventing them from coming into close contact and thus reducing the likelihood of ACQ.

To select the optimal concentration of Zn-TCPP-MOF for detection, fluorescence values were measured as a function of different concentrations of Zn-TCPP-MOF aqueous solutions. The scanning results showed that 1 mg mL<sup>-1</sup> MOF solution exhibited the highest and most stable fluorescence over a duration of 1 h.

An excitation emission matrix (EEM) is a 3D scan obtained during the measurement of the fluorescence of a sample when irradiated with UV or visible light. The data from EEM can be represented in a contour plot of excitation wavelength *vs.* emission wavelength *vs.* fluorescence intensity. EEMs are useful for studying multi-component systems and provide a molecular fingerprint for different types of samples. To distinguish between the luminescent properties of the prepared pure Zn-TCPP MOF and the Zn-TCPP@Trastuzumab biosensor, the EEM for both was measured at excitation wavelengths (450–390 nm), and the range of emission wavelength was 550–750 nm. Results are shown in Fig. 5. The maximum emission wavelength was in the red region at 660 nm, and the corresponding optimum excitation wavelength was 415 nm. We observed a similar EEM in the case of Zn-TCPP@Trastuzumab biosensor with slight quenching, which may be attributed to the fact that the binding of antibodies to the MOF cause the static quenching of fluorescence. In a static quenching, the quencher binds

to the fluorophore in its ground state, forming a complex that does not undergo the excited state transitions necessary for fluorescence emission. This binding interaction can occur through various forces, including van der Waals forces, hydrogen bonding, or hydrophobic interactions.<sup>52</sup>

TCSPC provides a decay curve representing the number of photons detected at different times after the excitation pulse at 415 nm and emission at 620 nm. By fitting this decay curve to an exponential model, fluorescence lifetime(s) of the MOF can be extracted. It was found that pure MOF and antibody-attached MOF have very similar lifetimes of 0.58 and 0.53 nanoseconds, respectively, as shown in Fig. S11.† In addition, the FL lifetimes of MOF before and after the protein addition did not change significantly, which indicated that the FL quenching could be attributed to a static quenching process in the ground state.

We speculated that this may be on account of the fact that the Zn atom in MOF might be combined with the amino group in proteins to form a nonfluorescent structure.<sup>53</sup> Zn-TCPP is a fluorescent MOF when it attaches to a protein and undergoes static quenching, which typically implies that the fluorophore ligand (TCPP) within the MOF forms a non-fluorescent complex with the protein. Moreover, static quenching occurs when the fluorophore within the MOF and the protein forms a stable complex in the ground state before the fluorophore is excited. This complex is non-fluorescent. The quenching is due to specific interactions between the MOF and the protein, such as hydrogen bonding, van der Waals forces, hydrophobic interactions, or covalent bonding. In the non-fluorescent complex, the energy that would usually be emitted as fluorescence is dissipated through non-radiative pathways. This implies that the energy of the fluorophore is transferred to the protein in a manner that does not result in photon emission.

To achieve the highest performance of the immunosensor, the detection environments were tested in aqueous media as a function of the biosensor concentration. Fluorescence measurements of the biosensor without the antigen were repeated to determine the highest fluorescence that can be

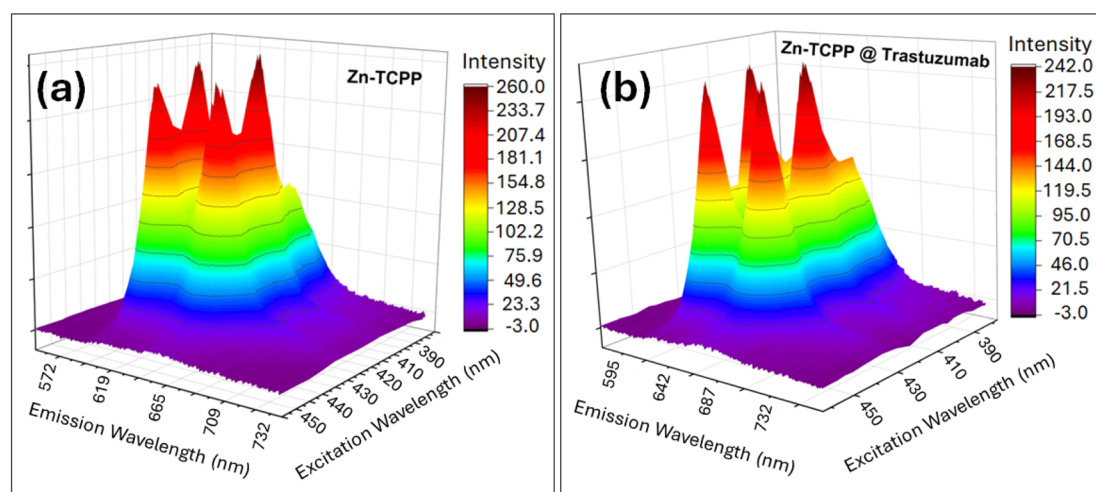


Fig. 5 EEM spectra of Zn-TCPP (a) nanosheets and (b) Zn-TCPP@Trastuzumab.





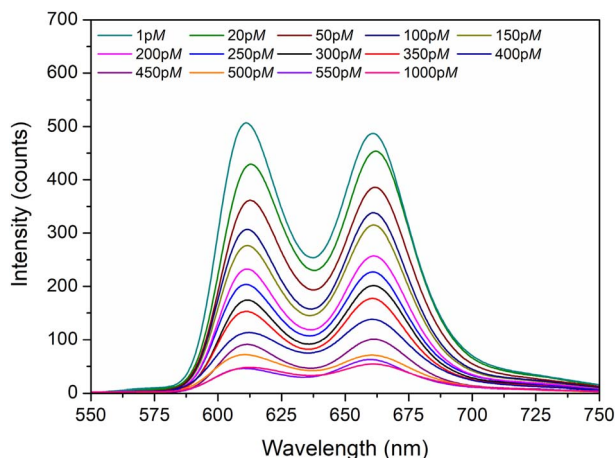


Fig. 6 FL emission spectra of the Zn-TCPP@Trastuzumab biosensor in the presence of different concentrations of HER2.

obtained. Deionized water was chosen to perform the immunoassay to simulate real samples from the body fluid environment. Additionally, the fluorescence of the biosensor in water was compared with that in other solvents, such as ethanol, acetone, and methanol, during the photoluminescence experiments. To select the optimal concentration of Zn-TCPP-MOF for detection, we performed the time scans of fluorescence intensity with different Zn-TCPP-MOF solution concentrations. The scanning results shown in Fig. 6 indicated that a 2.5 mg mL<sup>-1</sup> concentration of the biosensor solution had the highest fluorescence intensity, which was also the most stable fluorescence within a 1 h duration.

The implementation of this methodology has provided us with a novel approach for detecting the HER2 antigen. As shown in Fig. 6, in the Zn-TCPP@Trastuzumab biosensor with a concentration of 0.25 mg mL<sup>-1</sup>, the fluorescence emission intensities gradually decreased with the increase in HER2 concentration from 1 Pg mL<sup>-1</sup> to 500 Pg mL<sup>-1</sup>. Fig. S12† demonstrates a linear fitting curve of different concentrations of HER2, which quantitatively estimates the fluorescence quenching of the Zn-TCPP@Trastuzumab solution. In addition, the Stern–Volmer (SV) equation was utilized to describe the FL quenching:

$$(F_0/F) = 1 + K_{sv} [M]$$

$F_0$  and  $F$  are the luminescence intensities of Zn-TCPP@Trastuzumab in water at the emission wavelength of 660 nm before and after adding HER2,  $K_{sv}$  is the quenching constant and  $[M]$  represents the molar concentration of the HER2 antigen. Fig. S12† displays the correlation between  $\ln[F_0/F]$  and  $[M]$ . The  $F_0/F$  value is linearly related to the antigen concentration, and the  $K_{sv}$  value of the antigen is 0.354 pM<sup>-1</sup>, which is directly related to the sensitivity of the fluorescence quenching. Notably, the sensitivity of the biosensor maintained a linear performance up to a concentration of 350 pg mL<sup>-1</sup>, while at higher concentrations, the sensitivity of the biosensor decreased. According to the standard deviation (SD) and limit of detection (LOD) formula ( $LOD = 3SD/K_{sv}$ ), the LOD value of Zn-TCPP@Trastuzumab against HER2 was 1.38 pM (picomolar) with  $R^2 = 0.9829$ , where  $r$  is the regression coefficient.<sup>54</sup> Table 1 shows a comparison of the LOD of other nanostructures used for HER2 sensing. It is evident that the performance of the currently evaluated Zn-TCPP@Trastuzumab nanostructure as a sensor for HER2 is higher than that achieved by similar nanostructures. This can be attributed to the 2D morphology of the Zn-TCPP flakes, where the immobilization of Trastuzumab onto their surfaces facilitates the interaction with the HER2 molecule, and hence a higher efficiency of detection. The relationship between HER2 at concentrations higher than 350 Pg mL<sup>-1</sup> (400, 450, 500, 550 and 1000 pg mL<sup>-1</sup>) and luminescence properties of the Zn-TCPP biosensor was also evaluated. A non-linear relationship was observed, indicating the potential of Zn-TCPP@Trastuzumab as a biosensor for detecting HER2 at low concentrations (up to 350 pg mL<sup>-1</sup>) with high sensitivity.

#### Potential mechanism of HER2 detection using the Zn-TCPP@Trastuzumab biosensor

In this study, the drop in fluorescence intensity of the biosensor (Zn-TCPP@Trastuzumab) upon the addition of HER2 indicates the interaction between the fluorescent probe and the analyte. The quenching mechanism is elucidated based on the explanation given below. Generally, quenching of a fluorescent probe by an analyte can occur through several mechanisms: (1) Fluorescence Resonance Energy Transfer (FRET), (2) Inner Filter Effect (IFE), where the analyte absorbs the incident light instead of the fluorophore, and (3) dynamic or static quenching mechanisms. Spectroscopic UV-vis absorbance measurements

Table 1 Comparison of the LOD of various nanostructures used for detection of HER2

Biosensor type	Detection method	LOD	References
HER-AuNPs/antibodies (ELISA-Ab)	Electrochemical amperometric	1.060 pg mL <sup>-1</sup>	55
AuNPs/carbon nanotubes/screen printed electrode	Electrochemical amperometric	4.4 pg mL <sup>-1</sup>	56
HER2 antibodies immobilized on PbSQDs	Electrochemical voltammetric	280 pg mL <sup>-1</sup>	57
Graphene quantum nanoparticles/magnetic NPs	Fluorescence	1 cell per mL	58
Epitope-mediated molecularly imprinted polymers	SPR (Surface Plasmonic Resonance)	11.6 pg mL	59
PET/graphene nanomesh (GNM)/meso-SiO <sub>2</sub>	Field-effect transistors (FETs)	0.6 × 10 <sup>-15</sup> M	60
Molybdenum trioxide (MoO <sub>3</sub> ) anchored onto reduced graphene oxide (RGO)	Electrochemical	10 pg mL <sup>-1</sup>	61
Zn-TCPP@Trastuzumab	Fluorescence	1.38 pM	This work



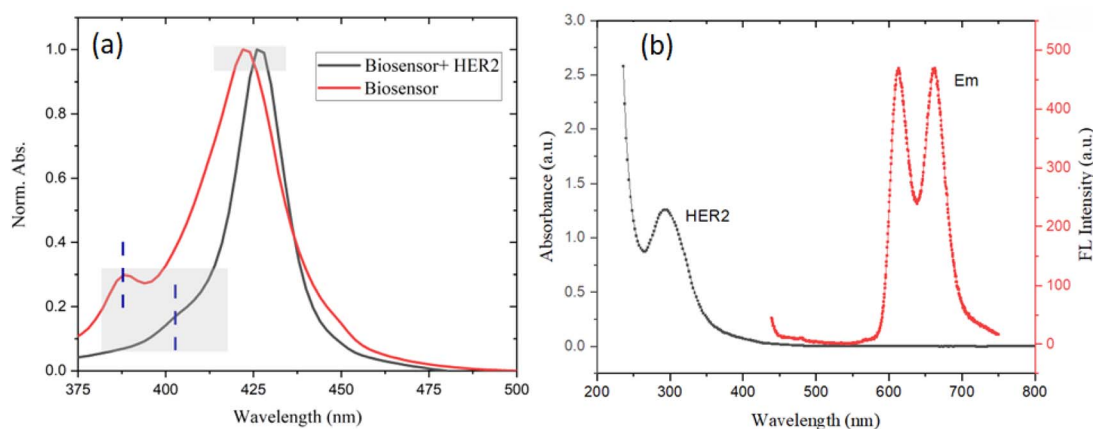


Fig. 7 (a) UV-vis spectra of the Zn-TCPP@Trastuzumab biosensor with and without interaction with HER2 and (b) UV-vis absorption spectra of HER2 and fluorescence emission spectrum of the Zn-TCPP@Trastuzumab biosensor.

for the biosensor were conducted both in the absence and presence of HER2. Fig. 7a represents the absorption spectra of the biosensor (Zn-TCPP@Trastuzumab) before and after adding the analyte (HER2), revealing the reduction of the characteristic absorption peak at 388 nm in the UV spectra of the biosensor upon the addition of HER2, indicating a significant interaction in the synthesized biosensor.<sup>62,63</sup> Furthermore, a red shift was observed in both absorbance peaks at 388 nm and 420 nm after adding the analyte. This shift indicates the change in the local electronic environment around the MOF.

Moreover, we tested the possibility of the FRET and IFE quenching mechanisms. Fig. 7b shows the emission spectrum of the biosensor and the absorption spectrum of HER2. Clearly, there is no overlap between these two spectra, which excludes the possibility of quenching *via* fluorescence resonance energy transfer (FRET), which primarily relies on the efficient energy transfer from the donor's excited state to the acceptor's excited state.<sup>43</sup> At the same time, there is no absorption of incident light needed for biosensor excitation by the analyte, ruling out the possibility of the inner filter effect (IFE).<sup>63</sup>

In order to further verify the static quenching mechanism, the Stern-Volmer plot was considered. The fluorescence quenching mechanism was attributed to static quenching, which can be verified by the Stern-Volmer equation:

$$(F_0/F) = 1 + K_{sv} C_q = 1 + K_q \tau_0 C_q$$

here,  $F_0$  and  $F$  denote the fluorescence intensities at 660 nm in the absence and presence of the quencher, respectively.  $K_{sv}$  is the Stern-Volmer quenching constant, and  $C_q$  represents the molar concentration of the HER2 antigen.  $K_q$  and  $\tau_0$  are the quencher rate coefficient and lifetime of the fluorophore (Zn-TCPP@Trastuzumab biosensor), respectively.

As shown in the calibration curve in Fig. S12,† a linear relationship between  $F_0/F$  and  $C_q$  was observed, with a calculated  $K_{sv}$  value of  $3.54 \times 10^{11} \text{ M}^{-1}$ , and the life time of biosensor was measured to be 0.53 ns from lifetime measurements; thus, the quenching rate coefficient  $K_q$  was determined to be  $6.68 \times 10^{20} \text{ M}^{-1} \text{ s}^{-1}$ , which exceeds the theoretical limit for dynamic

quenching ( $1.0 \times 10^{10} \text{ M}^{-1} \text{ s}^{-1}$ ). This result confirms that the fluorescence quenching is predominantly governed by a static quenching mechanism.<sup>64</sup>

Overall, the quenching of the biosensor is attributed to the aggregation of proteins, which induces conformational changes, resulting in the formation of a ground-state complex between the biosensor and the protein. This complex prevents fluorescence emission through static quenching, where the interaction occurs in the ground state of both the biosensor and the protein, reducing fluorescence by forming a non-fluorescent complex.

It is crucial to determine the sensor's ability to exhibit exceptional selectivity without interference from other possible interfering biomolecules. Hence, the selectivity of the suggested biosensor was assessed by measuring the PL response of the

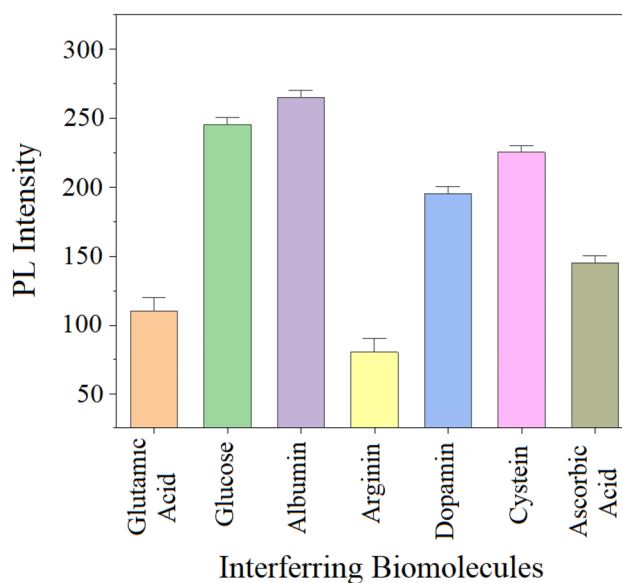
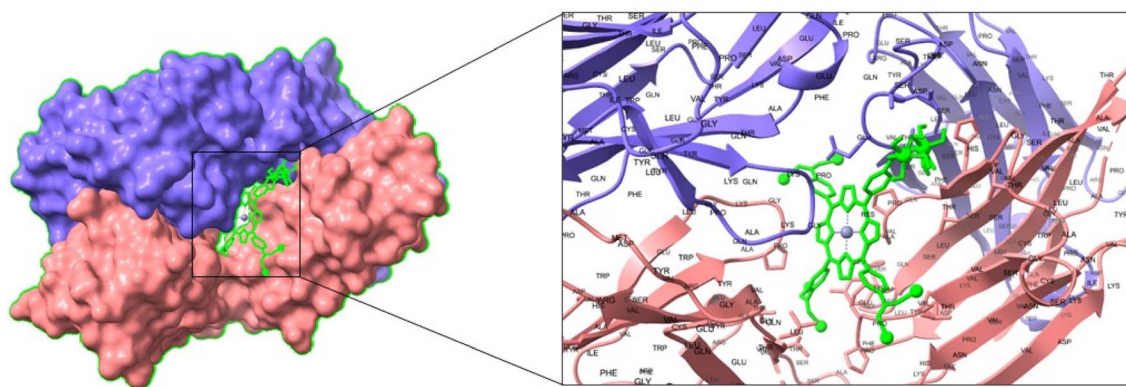


Fig. 8 Fluorescence intensity of Zn-TCPP@Trastuzumab before and after the introduction of various biological compounds and the HER2 antigen.



**Table 2** Photoluminescence (PL) intensity and relative standard deviation (RSD) values of the biosensor detecting HER2 antigen at a concentration of 150 pg mL<sup>-1</sup>, both before and after the introduction of various interferents

	Glutamic acid	Glucose	Albumin	Arginine	Dopamine	Cysteine	Ascorbic acid	Blank
Average	108.3333	245	265	109	195	225	145	275
SD	2.8868	5	5	3.6056	5	5	5	5
RSD	2.6647	2.0408	1.8868	3.3078	2.5641	2.2222	3.4483	1.8182

**Scheme 2** Surface view showing the interaction between protein (Trastuzumab) and Zn-TCPP SBU, with an enlarged image of the binding groove showing amino acid residues involved in molecular interactions.

biosensor in the presence of interfering proteins and other molecules, which can be present in the body. Those included glutamic acid, glucose, albumin, arginine, dopamine, cysteine, and ascorbic acid, along with the HER2 antigen, with a concentration of 150 Pg mL<sup>-1</sup>, which shows the fluorescence of ~275 (a.u.). All samples were measured under the same conditions, and their PL responses are illustrated in Fig. 8. The average values and relative standard deviation (RSD) data of PL upon the addition of different interferents are displayed in Table 2. As shown in Fig. 8, the fluorescence intensity had no recognizable change in the presence of four interfering molecules (150 pg mL<sup>-1</sup>). However, the addition of arginine, ascorbic acid, and glutamic acid (150 pg mL<sup>-1</sup>) affected the sensitivity of the biosensor, where a noticeable decrease in the PL response was observed. These results suggest that the proposed biosensor could be affected by the acidity of some molecules. Acidic biomolecules are believed to interact with the MOF structure, leading to the breakdown of its hierarchical structure. Therefore, it is highly recommended to maintain the pH of the sample in the neutral range to ensure an accurate result.

The highly stable bonding between the metal ions and organic linkers results in the subsequent formation of a stable geometry and rigid framework. In these structures, both the metal ions and the organic linkers have fixed positions. The SBU of the MOF can be a good representative of MOF in computational studies, as it is considered the basic unit for Zn-TCPP, *i.e.*, the joining of these SBUs to one another produces the 3D structure of Zn-TCPP. A typical SBU of Zn-TCPP, consisting of four zinc ion paddle wheels linked to a single TCPP molecule, was chosen for studying the interaction of Zn-TCPP and

Trastuzumab. The 3D structure of Trastuzumab contains two main chains: A and B. They show the presence of mostly beta sheets. The complex of Trastuzumab with Zn-TCPP SBU indicates that MOF fits in the cavity between the two chains, as shown in Scheme 2. The values for interfacial area and atomic contact energy were calculated to be 628.40 Å<sup>2</sup> and -368.41 kcal mol<sup>-1</sup>, respectively, indicating strong binding. It is believed that many amino acid residues along the Trastuzumab protein are involved in binding (Pro 174, 41, Leu 115, Gly 42, Glu 155165). The amino acid residues, Leu and Pro, have hydrophobic side chains and are directed to the benzene rings of the SBU structure; whereas Glu has negatively charged groups, and hence it may be attracted to the zinc ions. It can be inferred that the binding between the Zn-TCPP SBU unit and Trastuzumab is primarily due to hydrophobic interactions, with a possibility of minor contribution from electrostatic interactions.

## Conclusions

Recent research has shown that using a fluorescent Zn-TCPP MOF bioconjugated with trastuzumab antibodies for a straightforward yet exceptionally effective approach to the biosensing of HER2, a cancer biomarker, is promising. The use of Zn-TCPP MOF as a sensing material for detecting cancer biomarkers is unique due to several key advantages over alternative fluorescent nanomaterials, such as organic dyes and quantum dots. Notably, Zn-TCPP is free of any harmful elements and provides a consistent and reliable fluorescence signal. In contrast to other nanomaterials, Zn-TCPP does not



necessitate post-synthesis modifications or the addition of a secondary layer before attaching antibodies. When compared to existing fluorescent immunosensors for HER2, the Zn-TCPP@Trastuzumab biosensor exhibited performance that is either superior or on par with them in terms of both the analytical range and the limit of detection. This system demonstrated exceptional sensitivity and moderate specificity. The proposed biosensing approach, involving the conjugation of antibodies and MOF, can be further expanded for the development of bioimaging systems to detect various types of *in vivo* HER2-positive cancers.

## Data availability

These data can be obtained free of charge via [https://www.ccdc.cam.ac.uk/data\\_request/cif](https://www.ccdc.cam.ac.uk/data_request/cif), by emailing [data\\_request@ccdc.cam.ac.uk](mailto:data_request@ccdc.cam.ac.uk), or by contacting the Cambridge Crystallographic Data Centre, 12 Union Road, Cambridge CB2 1EZ, UK; fax: +44 1223 336033.

## Conflicts of interest

There are no conflicts to declare.

## Acknowledgements

The authors acknowledge financial support from the UAEU research office and the Zayed Centre for Health Sciences (ZCHS\_UAEU) (Grant # 12R077).

## References

- 1 M. R. Ibrahim and Y. E. Greish, MOF-Based Biosensors for the Detection of Carcinoembryonic Antigen: A Concise Review, *Molecules*, 2023, **28**, 5970.
- 2 J. T. Gohring, P. S. Dale and X. Fan, Detection of HER2 Breast Cancer Biomarker Using the Opto-Fluidic Ring Resonator Biosensor, *Sens. Actuators, B*, 2010, **146**, 226–230.
- 3 N. Shahbazi, R. Zare-Dorabei and S. M. Naghib, Design of a Ratiometric Plasmonic Biosensor for Herceptin Detection in HER2-Positive Breast Cancer, *ACS Biomater. Sci. Eng.*, 2022, **8**, 871–879.
- 4 Z. M. Lah, S. A. A. Ahmad, M. S. Zaini and M. A. Kamarudin, An Electrochemical Sandwich Immunosenor for the Detection of HER2 Using Antibody-Conjugated PbS Quantum Dot as a Label, *J. Pharm. Biomed. Anal.*, 2019, **174**, 608–617.
- 5 P. Mehrotra, Biosensors and Their Applications - A Review, *J. Oral Biol. Craniofac. Res.*, 2016, **6**, 153–159.
- 6 A. Ghosh, S. Fathima Thanutty Kallungal and S. Ramaprabhu, 2D Metal–Organic Frameworks: Properties, Synthesis, and Applications in Electrochemical and Optical Biosensors, *Biosensors*, 2023, **13**, 123.
- 7 M. T. Ulhakim, M. Rezki, K. K. Dewi, S. A. Abrori, S. Harimurti, N. L. W. Septiani, K. A. Kurnia, W. Setyaningsih, N. Darmawan and B. Yuliarto, Recent Trend on Two-Dimensional Metal–Organic Frameworks for Electrochemical Biosensor Application, *J. Electrochem. Soc.*, 2020, **167**, 136509.
- 8 S. Wang, M. Wang, C. Li, H. Li, C. Ge, X. Zhang and Y. Jin, A Highly Sensitive and Stable Electrochemiluminescence Immunosensor for Alpha-Fetoprotein Detection Based on Luminol-AgNPs@Co/Ni-MOF Nanosheet Microflowers, *Sens. Actuators, B*, 2020, **311**, 127919.
- 9 Y. Wang, Z. Mao, Q. Chen, K. Koh, X. Hu and H. Chen, Rapid and Sensitive Detection of PD-L1 Exosomes Using Cu-TCPP 2D MOF as an SPR Sensitizer, *Biosens. Bioelectron.*, 2022, **201**, 113954.
- 10 N. Zhu, L. Gu, J. Wang, X. Li, G. Liang, J. Zhou and Z. Zhang, Novel and Sensitive Chemiluminescence Sensors Based on 2D-MOF Nanosheets for One-Step Detection of Glucose in Human Urine, *J. Phys. Chem. C*, 2019, **123**, 9388–9393.
- 11 G. Xiong, Q. Li, L. Liang, X. Zhang, K. Huang and D. Qin, Constructing a 3D zinc metal–organic framework for ratiometric and selectively  $\text{PO}_4^{3-}$  sensing and catalyzing  $\text{CO}_2$  chemical fixation, *J. Molecular Structure*, 2025, **1321**, 139725.
- 12 W. Xu, S. Xu, X. Zhang, K. Huang, L. Liang and D. Qin, AIE pyrene-based luminescence zinc MOF for selective and sensitive ATP and ADP sensing in water by analyte-induced structure decomposition, *Microchem. J.*, 2024, **207**, 111866.
- 13 S. E. Miller, M. H. Teplensky, P. Z. Moghadam and D. Fairen-Jimenez, Metal–Organic Frameworks as Biosensors for Luminescence-Based Detection and Imaging, *Interface Focus*, 2016, **6**, 20160027.
- 14 D. Yan, Y. Lou, Y. Yang, Z. Chen, Y. Cai, Z. Guo, H. Zhan and B. Chen, Dye-Modified Metal–Organic Framework as a Recyclable Luminescent Sensor for Nicotine Determination in Urine Solution and Living Cell, *ACS Appl. Mater. Interfaces*, 2019, **11**, 47253–47258.
- 15 S. Qu, Z. Li and Q. Jia, Detection of Purine Metabolite Uric Acid with Picolinic-Acid-Functionalized Metal–Organic Frameworks, *ACS Appl. Mater. Interfaces*, 2019, **11**, 34196–34202.
- 16 H. Yu, M. Fan, Q. Liu, Z. Su, X. Li, Q. Pan and X. Hu, Two Highly Water-Stable Imidazole-Based Ln-MOFs for Sensing  $\text{Fe}^{3+}$ ,  $\text{Cr}_2\text{O}_7^{2-}/\text{CrO}_4^{2-}$  in a Water Environment, *Inorg. Chem.*, 2020, **59**, 2005–2010.
- 17 X. Zhang, Q. Zhang, D. Yue, J. Zhang, J. Wang, B. Li, Y. Yang, Y. Cui and G. Qian, Flexible Metal–Organic Framework-Based Mixed-Matrix Membranes: A New Platform for  $\text{H}_2\text{S}$  Sensors, *Small*, 2018, **14**, 1821563.
- 18 S. A. A. Razavi, M. Y. Masoomi and A. Morsali, Morphology-dependent sensing performance of dihydro-tetrazine functionalized MOF toward Al(III), *Ultrason. Sonochem.*, 2018, **41**, 17–26.
- 19 A. Sousaraei, C. Queiros, F. G. Moscoso, T. Lopes-Costa, J. M. Pedrosa, A. M. G. Silva, L. Cunha-Silva and J. Cabanillas-Gonzalez, Sub-ppm Amine Detection via Absorption and Luminescence Turn-On Caused by Ligand Exchange in Metal Organic Frameworks, *Anal. Chem.*, 2019, **91**, 15853–15859.
- 20 V. K. Maka, A. Mukhopadhyay, G. Savitha and J. N. Moorthy, Fluorescent 2D metal–organic framework nanosheets





- (MONs): design, synthesis and sensing of explosive nitroaromatic compounds (NACs), *Nanoscale*, 2018, **10**, 22389–22399.
- 21 L.-J. Han, D. Zheng, S.-G. Chen, H.-G. Zheng and J. Ma, A Highly Solvent-Stable Metal–Organic Framework Nanosheet: Morphology Control, Exfoliation, and Luminescent Property, *Small*, 2018, **14**, 1703873.
  - 22 J.-Z. Wei, X.-L. Wang, X.-J. Sun, Y. Hou, X. Zhang, D.-D. Yang, H. Dong and F.-M. Zhang, Rapid and Large-Scale Synthesis of IRMOF-3 by Electrochemistry Method with Enhanced Fluorescence Detection Performance for TNP, *Inorg. Chem.*, 2018, **57**, 3818–3824.
  - 23 L. Yang, Y. Song and L. Wang, Multi-emission metalorganic framework composites for multicomponent ratiometric fluorescence sensing: recent developments and future challenges, *J. Mater. Chem. B*, 2020, **8**, 3292–3315.
  - 24 S. Wu, H. Min, W. Shi and P. Cheng, Multicenter Metal–Organic Framework-Based Ratiometric Fluorescent Sensors, *Adv. Mater.*, 2020, **32**, 1805871.
  - 25 L. Chen, D. Liu, J. Peng, Q. Du and H. He, Ratiometric fluorescence sensing of metal–organic frameworks: tactics and perspectives, *Coord. Chem. Rev.*, 2019, **404**, 213113.
  - 26 C. Li, J. Hai, S. Li, B. Wang and Z. Yang, Luminescent magnetic nanoparticles encapsulated in MOFs for highly selective and sensitive detection of  $\text{ClO}^-/\text{SCN}^-$  and anticounterfeiting, *Nanoscale*, 2018, **10**, 8667–8676.
  - 27 P. Das and S. K. Mandal, Strategic Design and Functionalization of an Amine-Decorated Luminescent Metal Organic Framework for Selective Gas/Vapor Sorption and Nanomolar Sensing of 2,4,6-Trinitrophenol in Water, *ACS Appl. Mater. Interfaces*, 2018, **10**, 25360–25371.
  - 28 L. Guo, M. Liang, X. Wang, R. Kong, G. Chen, L. Xia and F. Qu, The role of l-histidine as molecular tongs: a strategy of grasping  $\text{Tb}^{3+}$  using ZIF-8 to design sensors for monitoring an anthrax biomarker on-the-spot, *Chem. Sci.*, 2020, **11**, 2407–2413.
  - 29 R. Dalapati and S. Biswas, A Pyrene-Functionalized Metal–Organic Framework for Nonenzymatic and Ratiometric Detection of Uric Acid in Biological Fluid via Conformational Change, *Inorg. Chem.*, 2019, **58**, 5654–5663.
  - 30 H. Pan, S. Wang, X. Dao and Y. Ni, Fluorescent Zn-PDC/ $\text{Tb}^{3+}$  Coordination Polymer Nanostructure: A Candidate for Highly Selective Detections of Cefixime Antibiotic and Acetone in Aqueous System, *Inorg. Chem.*, 2018, **57**, 1417–1425.
  - 31 J. Chen, Y. Zhu and S. Kaskel, Porphyrin-Based Metal–Organic Frameworks for Biomedical Applications, *Angew. Chem., Int. Ed.*, 2021, **60**, 5010–5035.
  - 32 Y. Pang, Y. Cao, J. Han, Y. Xia, Z. He, L. Sun and J. Liang, A Novel Fluorescence Sensor Based on Zn Porphyrin MOFs for the Detection of Bisphenol A with High Selectivity and Sensitivity, *Food Control*, 2022, **132**, 108551.
  - 33 J. Bao, J. Mei, X. Cheng, D. Ren, G. Xu, F. Wei, Y. Sun, Q. Hu and Y. Cen, A Ratiometric Lanthanide-Free Fluorescent Probe Based on Two-Dimensional Metal–Organic Frameworks and Carbon Dots for the Determination of Anthrax Biomarker, *Microchim. Acta*, 2021, **188**, 84.
  - 34 J. Ma, W. Bai and J. Zheng, A Novel Self-Cleaning Electrochemical Biosensor Integrating Copper Porphyrin-Derived Metal–Organic Framework Nanofilms, G-Quadruplex, and DNA Nanomotors for Achieving Cyclic Detection of Lead Ions, *Biosens. Bioelectron.*, 2022, **197**, 113801.
  - 35 Y. Zhao, L. Jiang, L. Shangguan, L. Mi, A. Liu and S. Liu, Synthesis of Porphyrin-Based Two-Dimensional Metal–Organic Framework Nanodisk with Small Size and Few Layers, *J. Mater. Chem. A*, 2018, **6**, 2828–2833.
  - 36 S. Ito, F. J. White, E. Okunishi, Y. Aoyama, A. Yamano, H. Sato, J. D. Ferrara, M. Jasnowski and M. Meyer, Structure Determination of Small Molecule Compounds by an Electron Diffractometer for 3D ED/MicroED, *CrystEngComm*, 2021, **23**, 8622–8630.
  - 37 K.-N. Truong, S. Ito, J. M. Wojciechowski, C. R. Göb, C. J. Schürmann, A. Yamano, M. Del Campo, E. Okunishi, Y. Aoyama, T. Mihira, N. Hosogi, J. Benet-Buchholz, E. C. Escudero-Adán, F. J. White, J. D. Ferrara and R. Bücker, Making the Most of 3D Electron Diffraction: Best Practices to Handle a New Tool, *Symmetry*, 2023, **15**, 1555.
  - 38 N. Sadeghi, S. Sharifnia and M. A. Sheikh Arabi, A Porphyrin-Based Metal Organic Framework for High-Rate Photoreduction of  $\text{CO}_2$  to  $\text{CH}_4$  in Gas Phase, *J. CO<sub>2</sub> Util.*, 2016, **16**, 450–457.
  - 39 L. Wang, P. Jin, S. Duan, J. Huang, H. She, Q. Wang and T. An, Accelerated Fenton-Like Kinetics by Visible-Light-Driven Catalysis Over Iron(III) Porphyrin Functionalized Zirconium MOF: Effective Promotion on the Degradation of Organic Contaminants, *Environ. Sci.: Nano*, 2019, **6**, 2652–2661.
  - 40 Rigaku Oxford Diffraction, CrysAlisPro Software System, Rigaku Corporation, Wrocław, Poland, 2023, version 1.171.43.76a.
  - 41 G. M. Sheldrick, SHELXT – Integrated Space-Group and Crystal-Structure Determination, *Found. Adv.*, 2015, **71**, 3–8.
  - 42 G. M. Sheldrick, Crystal Structure Refinement with SHELXL, *Struct. Chem.*, 2015, **71**, 3–8.
  - 43 Rigaku Oxford Diffraction, AutoChem 6 Software System in Conjunction with OLEX2, Rigaku Corporation, Wrocław, Poland, 2023, version 1.5-ac6-009.
  - 44 O. V. Dolomanov, L. J. Bourhis, R. J. Gildea, J. A. K. Howard and H. O. Puschmann, OLEX2: A Complete Structure Solution, Refinement, and Analysis Program, *J. Appl. Cryst.*, 2009, **42**, 339–341.
  - 45 F. L. Hirshfeld, Can X-ray Data Distinguish Bonding Effects from Vibrational Smearing?, *Acta Crystallogr., Sect. A*, 1976, **32**, 239–244.
  - 46 A. Thorn, B. Dittrich and G. M. Sheldrick, Enhanced Rigid-Bond Restraints, *Acta Crystallogr., Sect. A: Found. Crystallogr.*, 2012, **68**, 448–451.
  - 47 A. Urtizberea, E. Natividad, P. J. Alonso, M. A. Andrés, I. Gascón, M. Goldmann and O. Roubeau, A Porphyrin Spin Qubit and Its 2D Framework Nanosheets, *Adv. Funct. Mater.*, 2018, **28**, 1801695.



- 48 Z.-H. Zhu, Y. Liu, C. Song, Y. Hu, G. Feng and B. Z. Tang, Porphyrin-Based Two-Dimensional Layered Metal–Organic Framework with Sono-/Photocatalytic Activity for Water Decontamination, *ACS Sens.*, 2021, **16**, 1346–1357.
- 49 Z. Zhou, S. Mukherjee, J. Warnan, W. Li, S. Wannapaiboon, S. Hou, K. Rodewald, B. Rieger, P. G. Weidler, C. Wöll and R. A. Fischer, Porphyrin-Based Metal–Organic Framework Films: Nucleation and Growth, *J. Mater. Chem. A*, 2020, **8**, 25941–25950.
- 50 M. Zhao, Y. Wang, Q. Ma, Y. Huang, X. Zhang, J. Ping, Z. Zhang, Q. Lu, Y. Yu, H. Xu, Y. Zhao and H. Zhang, Ultrathin 2D Metal–Organic Framework Nanosheets, *Adv. Mater.*, 2015, **27**, 7372–7378.
- 51 N. Bhardwaj, S. K. Bhardwaj, J. Mehta, M. K. Nayak and A. Deep, Bacteriophage Conjugated IRMOF-3 as a Novel Opto-Sensor for *S. arlettae*, *New J. Chem.*, 2016, **40**, 8068–8073.
- 52 W. Shou, F. Kang and J. Lu, Nature and Value of Freely Dissolved EPS Ecosystem Services: Insight into Molecular Coupling Mechanisms for Regulating Metal Toxicity, *Environ. Sci. Technol.*, 2018, **52**, 457–466.
- 53 J. Hou, P. Jia, K. Yang, T. Bu, S. Zhao, L. Li and L. Wang, Fluorescence and Colorimetric Dual-Mode Ratiometric Sensor Based on Zr–Tetraphenylporphyrin Tetrasulfonic Acid Hydrate Metal–Organic Frameworks for Visual Detection of Copper Ions, *ACS Appl. Mater. Interfaces*, 2022, **14**, 13848–13857.
- 54 Y. Pang, Y. Cao, J. Han, Y. Xia, Z. He, L. Sun and J. Liang, A Novel Fluorescence Sensor Based on Zn Porphyrin MOFs for the Detection of Bisphenol A with High Selectivity and Sensitivity, *Food Control*, 2022, **132**, 108551.
- 55 S. Wignarajah, I. Chianella and I. E. Tothill, Development of Electrochemical Immunosensors for HER-1 and HER-2 Analysis in Serum for Breast Cancer Patients, *Biosensors*, 2023, **13**, 355.
- 56 Y. Makableh, T. Athamneh, M. Ajlouni, S. Hijazi and A. Alnaimi, Enhanced Response and Selective Gold Nanoparticles/Carbon Nanotubes Biosensor for the Early Detection of HER2 Biomarker, *Sens. Actuators Rep.*, 2023, **5**, 100158.
- 57 Z. M. Azizah, N. H. Lah, S. A. A. Ahmad, M. S. Zaini and M. A. Kamarudin, An Electrochemical Sandwich Immunosensor for the Detection of HER2 Using Antibody-Conjugated PbS Quantum Dot as a Label, *J. Pharm. Biomed. Anal.*, 2019, **174**, 608–617.
- 58 M. Dighehsaraei, M. Salouti, B. Amini, S. Mahmazi, M. Kalantari, A. Kazemizadeh and J. Mehrvand, Developing a Fluorescence Immunosensor for Detection of HER2-Positive Breast Cancer Based on Graphene and Magnetic Nanoparticles, *Microchem. J.*, 2021, **167**, 106300.
- 59 K. Erol, G. Hasabnis and Z. Altinatas, A Novel Nano MIP-SPR Sensor for Point-of-Care Diagnosis of Breast Cancer, *Micromachines*, 2023, **14**, 1086.
- 60 Y. Yang, X. Yang, X. Zou, S. Wu, D. Wan, A. Cao, L. Liao, Q. Yuan and X. Duan, Ultrafine Graphene Nanomesh with Large On/Off Ratio for High-Performance Flexible Biosensors, *Adv. Funct. Mater.*, 2017, **27**, 1604096.
- 61 S. Augustine, P. Kumar and B. D. Malhotra, Amine-Functionalized MoO<sub>3</sub>@RGO Nanohybrid-Based Biosensor for Breast Cancer Detection, *ACS Appl. Bio Mater.*, 2019, **2**, 5366–5378.
- 62 D. S. Ravindran, S. Mukundan and K. G. Kumar, A Simple and Efficient Turn-Off Fluorescence Sensor for the Nanomolar Detection of Homovanillic Acid Using Protein-Mediated Blue Emitting Nickel Nanoclusters, *ChemistrySelect*, 2021, **6**, 2477–2482.
- 63 P. Jia, Q. Wu, B. Sun and L. Wang, Formic Acid-Regulated Defect Engineering in Zr-Based Metal–Organic Frameworks toward Fluorescence Sensor for Sensitive Detection of Chlortetracycline, *Small*, 2023, **19**, 2304096.
- 64 J. Hou, P. Jia, K. Yang, T. Bu, S. Zhao, L. Li and L. Wang, Fluorescence and Colorimetric Dual-Mode Ratiometric Sensor Based on Zr–Tetraphenylporphyrin Tetrasulfonic Acid Hydrate Metal–Organic Frameworks for Visual Detection of Copper Ions, *ACS Appl. Mater. Interfaces*, 2022, **14**, 13848–13857.

